machines

MDPI

Article

Dynamic Service Mechanism of Double-Row Spherical Roller Bearings Due to Self-Aligning Behavior

Yu Xing [1], Yifei Zhang [2,*], Yin Zhang [3], Daoyun Qiao [3], Yuxia Pei [3] and Yuan Xiao [1]

[1] School of Mechanical and Electrical Engineering, Xi'an Polytechnic University, Xi'an 710048, China
[2] Key Laboratory of Expressway Construction Machinery of Shaanxi Province, Xi'an 710054, China
[3] State Key Laboratory of Smart Manufacturing for Special Vehicles and Transmission System, Baotou 014030, China
* Correspondence: zyf@chd.edu.cn

Abstract: Spherical roller bearings (SRBs) are widely used under self-aligning operating conditions, such as rotor bending or an angular misalignment between inner and outer rings due to their self-aligning function. However, the characterization of SRBs' self-aligning function is often ignored in the present models. The reason for this is that the self-aligning condition is essentially a fault condition, and many scholars have assumed SRBs are in an ideal operating condition. Although there is nothing wrong with this analysis theoretically, it is incapable of characterizing SRBs' service behavior comprehensively. In this work, the Lagrange equation was introduced to model the relationship among the rollers and the inner and outer rings. The contact region in particular was characterized in detail in order to solve the problems of undetermined contact status (UCS) and the varying law of the self-aligning contact angle (SAC angle). For the experiment, a novel SRBs pedestal with a self-aligning operating condition was designed, and the relevant self-aligning function testing was carried out. A good agreement was shown between the theoretical and experimental results. The results pointed out that, if taking no account of the self-aligning function, SRBs can be regarded as angular contact ball bearings or cylinder roller bearings. The amplitude of the inner-ring motion orbit is determined by the external load, but the shape is influenced by the direction and magnitude of the SAC angle. In the example of this paper, the values of the main frequency equal 136.8 Hz. Some additional frequencies are clearly aroused under the self-aligning operating condition, whose value is approximately equal to 8.3 Hz or its integer multiples. The dynamic performance of SRBs will be substantially improved by a light axial load plus an anticlockwise self-aligning contact angle rather than a large axial preload.

Keywords: spherical roller bearings; self-aligning behavior; self-aligning pedestal; dynamics; contact region characterization

Citation: Xing, Y.; Zhang, Y.; Zhang, Y.; Qiao, D.; Pei, Y.; Xiao, Y. Dynamic Service Mechanism of Double-Row Spherical Roller Bearings Due to Self-Aligning Behavior. *Machines* **2023**, *11*, 400. https://doi.org/10.3390/machines11030400

Academic Editor: César M. A. Vasques

Received: 19 December 2022
Revised: 10 January 2023
Accepted: 19 January 2023
Published: 19 March 2023

1. Introduction

Spherical roller bearings (SRBs) are widely used under low-speed, heavy-load, and self-aligning operating conditions, such as the main shaft of wind-power equipment, a rolling mill, and so on. The reason lies in the fact that SRBs can offset the additional bending moment due to the rotor bending by the spherical structure of the outer ring as well as the spheroidal rollers, shown in Figure 1. The spheroidal rollers in SRBs provide the self-aligning function. The generatrix of these rollers is a part of a sphere, but the rollers' macroscopic profile seems like a cylindrical one. These characteristics mean the contact region is a point or ellipse with a light external load. When the load is heavy, however, a line or rectangle (with a large length-to-width ratio) takes its place. So the magnitude of the external load is often regarded as the judgment of the SRB's contact status in the published references. Namely, Hertzian point-contact and line-contact theories are used to characterize contact regions with light and heavy loads, respectively.

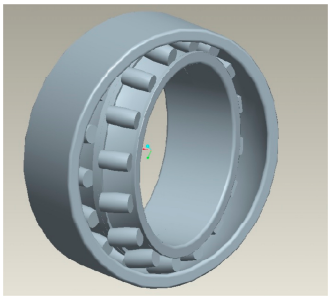

Figure 1. Double-row spherical roller bearing (short for SRB).

Bercea [1] established a static SRB model and clarified the contact status according to the magnitude of the external load. The SRBs' service performances due to surface defects, preload, and radial clearance were analyzed by Cao [2,3] based on Hertzian point-contact theory. A model used to characterize SRBs' dynamic performance under the light load operating condition was proposed by Ghalamchi [4], whose theoretical foundation is Hertzian point-contact theory too. The results revealed the pressure distribution as well as the relevant deformation of each roller. Ma [5] obtained the characteristic of load distribution with roller diameter deviation. Yang [6] pointed out the loading status of SRBs' roller, taking into account the self-aligning operating condition. A non-linear curve representing the relationship between the external load and roller deformation was fitted by Houpert [7] under the light-load operating condition. Additionally, Houpert [8] figured out that a transitional stage is essential between light-load and heavy-load conditions, which corresponds to a moderate external load. Specifically, the computing parameters in the transitional stage would be taking the place of those in the light-load or heavy-load stages.

In the authors' opinion, it is unreasonable since it is hard to find a proper criterion to determine light-load or heavy-load conditions. Although a transitional stage is added, an explicit criterion is also necessary to divide the regions among the light, moderate, and heavy load conditions. Furthermore, despite the large magnitude of the external load, the contact characteristic of the rollers in the minor supporting area remains point contact. At this moment, there are three kinds of contact status for all the rollers in a bearing, namely classical Hertzian point contact, line contact, and non-classical Hertzian contact. We named this phenomenon "undetermined contact status (UCS)" in the published paper [9]. And this viewpoint is accepted by the engineer of the bearing factory [10].

Despite the fact that the finite element method (FEM) can solve the above problem, for instance, Shah [11], Fiedler [12], Ciubotariu [13], Steininger [14], and Li [15] used commercial FEM software, such as ANSYS, Abaqus and so on, to simulate SRBs' contact status between rollers and raceways. However, meshing the contact region as well as the SRBs' components is complicated and costly in terms of computing rate. An experimental method proposed by Houpert [16,17], however, the given conclusion may be improper when the parameters are changed.

Furthermore, it is a type of malfunction for the SRB's self-aligning operating condition, which is derived from the misalignment between the inner and outer rings caused by rotor bending. Nonetheless, only a few studies on self-aligning operating conditions have been carried out. Shi [18] proposed a mathematical model with a flexible rotor and SRBs supporting it, whereby the maximum contact pressure was obtained. Although Ma [5] took into consideration the SRB's self-aligning function, the motion trends of all the rollers were consistent in his model, which is unreasonable. The reason lies in the fact that the direction and magnitude of self-aligning contact angles between rollers are different for each other. Yang [6] pointed out the influence of a self-aligning contact angle of varying magnitude and discussed SRBs' service performances under the rotor-bending operating condition. An asymmetric tube roll supported by SRBs was modeled by Heikkinen [19]. However, the influence caused by the varying contact angle was ignored, so the result is incomplete.

The evaluations about the direction and magnitude of SRBs' self-aligning contact angle are obtained according to the service performance of the bearings-rotor system, then modified in light of loading and SRBs' supporting methods. However, it either lacks the computing method of the SRB's self-aligning contact angle in particular or merely explains the influence due to the rotor bending in brief. A special software only used for SRBs analysis was developed by SKF company (Gothenburg, Sweden) which is named SPHERBEAN (SPHERical BEaring ANalysis) [20]. It is regarded as the most professional tool for SRB analysis, but the method of analysis is not available to the general public.

According to the preface, some existing problems are summarized briefly as: (a) the inability to characterize SRBs' self-aligning function, which contains not only the evaluation of self-aligning contact angle due to a bending rotor but also the contact status between each roller and the raceway; (b) the lack of an effective and simple dynamic model. A preferable method should be given to avoid FEM complexity, inconvenient extension of commercial software, and limitation of experimental results.

This paper is organized as follows: following the introduction, Section 2 introduced the Lagrange equation to model the relationship between SRB rollers and their inner and outer rings. The contact region, in particular, was characterized in detail on the basis of a non-Hertzian model in order to solve the problem of undetermined contact status (UCS) and the varying law of self-aligning contact angle. In Section 3, the experimental facility and testing method are proposed and established. Section 4 computed and analyzed the motion laws of the SRBs' components as well as their characteristic frequencies, both theoretically and experimentally. Furthermore, the impact of UCS and self-aligning contact angles was highlighted and discussed. In the Section 5, some conclusions and recommendations were made.

2. Mathematical Model

2.1. Fundamental Assumptions and Constitutive Equations

In light of the research contents, some fundamental assumptions are listed below.

The outer ring of the SRB is fixed, while the inner ring rotates with the rotor;

As shown in Figure 2, the Z direction is axial, while the X and Y directions are radial. To be specific, X is horizontal, and Y is vertical.

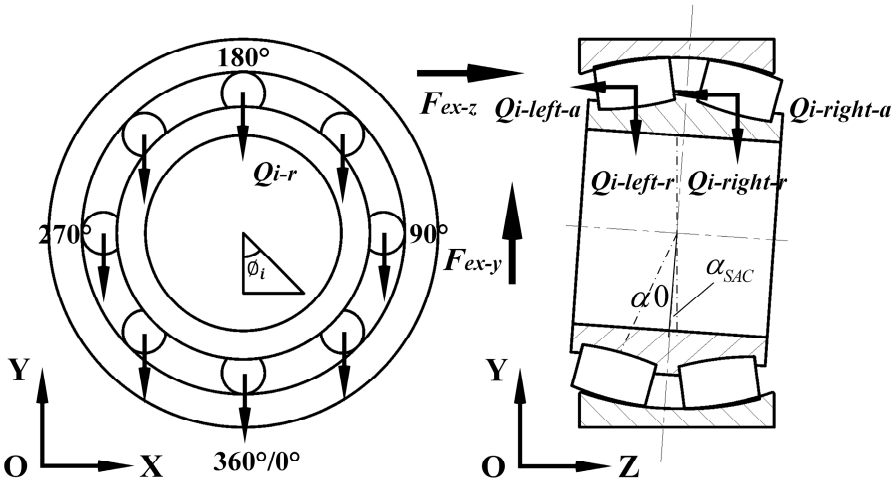

Figure 2. SRB schematic under global coordinate.

SRBs' self-aligning process is only emerging in the YOZ plane. Plus (+) means self-aligning clockwise, and minus (−) indicates an anticlockwise self-aligning process.

The contact between bearing components only occurs locally, and the contact parts are isotropic and uniform elastomers.

There is no slipping between the rollers and the raceway.

Lagrange equation is the constitutive equation to characterize the motion of SRBs' components [21], which is expressed as

$$\frac{d}{dt}\frac{\partial T}{\partial\left\{\dot{\xi}\right\}} - \frac{\partial T}{\partial\{\xi\}} + \frac{\partial V}{\partial\{\xi\}} = \{F\} \tag{1}$$

where t—time, s;
T—kinetic energy, Joule;
$\dot{\xi}$—velocity, mm/s, or rad/s;
ξ—displacement, mm;
V—potential energy, Joule;
F—external load, kN;
Theoretically, SRB components with kinetic energy include rollers, inner and outer rings, and the rotor. So the formulation of SRB's kinetic energy is written as

$$T = T_r + T_{out} + T_{in} + T_{rotor} \tag{2}$$

In Equation (2), each corner mark means that
r—roller;
out—outer ring;
in—inner ring.
There are two kinds of potential energy: gravitational potential energy, which comes from the gravity of each SRB component; and elastic potential energy, which is derived from elastic deformation between the roller and raceway. So the potential energy is defined as

$$V = V_r + V_{out} + V_{in} + V_{rotor} + V_{spring} \tag{3}$$

In Equation (3), the meaning of each corner mark is the same as before. V_{spring} is the elastic potential energy, whose unit is Joule.

2.2. Kinetic Energy and Gravitational Potential Energy for Each SRBs Components

The total kinetic energy of the rollers is the sum of the kinetic energy of each roller, which can be expressed as below

$$T_r = \sum_{row=1}^{2}\left(\sum_{i=1}^{Z} T_i\right) \tag{4}$$

where row—the number of the row;
Z—the number of the rollers;
i—the ith roller. The meanings of other symbols are the same as before.
The kinetic energy of the ith roller is written as

$$T_i = \frac{1}{2} m_i \dot{p}_i^{\,2} + \frac{1}{2} I_i \dot{\theta}_i^{\,2} \tag{5}$$

where m_i—the mass of the ith roller, kg;
$\dot{p}_i$—the linear velocity of the ith roller, mm/s;
I_i—the rotational inertia of the ith roller, kg·mm^2;
$\dot{\theta}_i$—the angular velocity of the ith roller, rad/s.
For each roller, its displacement is produced by the vibration along with the normal direction. The displacement can be decomposed under the global coordinate.

$$\vec{p}_i = \left(\vec{p}_i \cos(\phi_i)\cos(\alpha_i)\right)\hat{i} + \left(\vec{p}_i \sin(\phi_i)\cos(\alpha_i)\right)\hat{j} + \left(\vec{p}_i \sin(\alpha_i)\right)\hat{k} \tag{6}$$

where ϕ_i—the position angle of the ith roller, deg;

α_i—the contact angle of the ith roller, deg;
$\hat{i}, \hat{j}, \hat{k}$—the coordinate components in the X, Y, and Z directions, respectively.
Then for the ith roller, the linear velocity as well as its square is obtained easily.
It has been assumed the roller is rolling without slip, whereby the linear velocity of the global revolution is equal to that of autorotation. The relevant equation is defined as

$$R_{out}\left(\dot{\theta}_{out} - \dot{\phi}_i\right)\cos(\alpha_i) = -R_i\left(\dot{\theta}_i - \dot{\phi}_i\cos(\alpha_i)\right) \tag{7}$$

The relationship between revolution velocity and autorotation can be derived

$$\dot{\theta}_i = \dot{\phi}_i\cos(\alpha_i)\left(1 + \frac{R_{out}}{R_i}\right) \tag{8}$$

In Equations (7) and (8), R_{out}—the radius of the outer ring, mm;
$\dot{\theta}_{out}$—the autorotation angular velocity of the outer ring, rad/s;
$\dot{\theta}_i$—the autorotation angular velocity of the ith roller, rad/s;
$\dot{\phi}_i$—the global revolution angular velocity of the ith roller, rad/s, which can be obtained by the following equation

$$\dot{\phi}_i = \dot{\theta}_{rotor} \times \frac{R_{in}}{2 \times (R_{in} + R_i)} \tag{9}$$

$\dot{\theta}_{rotor}$—the velocity of the rotor, rpm;
R_{in}—the radius of the inner ring, mm;
R_i—the radius of the ith roller, mm.
The kinetic energy of each roller is derived by combining Equations (6)–(9) into the Equation (5).
The direction of roller gravity is the same as the Y direction in Figure 2, so the gravitational potential energy of each roller is defined as

$$V_i = m_i g p_i \sin(\phi_i)\cos(\alpha_i) \tag{10}$$

It has assumed the outer ring is fixed, whereby its kinetic energy and gravitational potential energy are all equal to 0.
The kinetic energy of the inner ring and rotor consists of two parts, namely non-linear vibration and autorotation, which are similar to the rollers. The relevant expression is given as below

$$T_{in} = \frac{1}{2}m_{in}\left(\dot{x}_{in}^2 + \dot{y}_{in}^2 + \dot{z}_{in}^2\right) + \frac{1}{2}I_{in}\dot{\theta}_{in}^2 \tag{11}$$

$$T_{rotor} = \frac{1}{2}m_{rotor}\left(\dot{x}_{rotor}^2 + \dot{y}_{rotor}^2 + \dot{z}_{rotor}^2\right) + \frac{1}{2}I_{rotor}\dot{\theta}_{rotor}^2 \tag{12}$$

where m_{in}, m_{rotor}—the mass of the inner ring and rotor, kg;
$\dot{x}_{in}, \dot{x}_{rotor}$—the velocity of the inner ring and the rotor in X direction, mm/s;
$\dot{y}_{in}, \dot{y}_{rotor}$—the velocity of the inner ring and the rotor in Y direction, mm/s;
$\dot{z}_{in}, \dot{z}_{rotor}$—the velocity of the inner ring and the rotor in Z direction, mm/s;
I_{in}, I_{rotor}—the rotational inertia of the inner ring and the rotor, kg·mm^2;
$\dot{\theta}_{in}, \dot{\theta}_{rotor}$—the autorotation angular velocity of the inner ring and the rotor, rad/s.
The displacement of the inner ring equals that of the rotor since they have synchronous movement.

$$\begin{aligned} x_{in} &= x_{rotor} \\ y_{in} &= y_{rotor} \\ z_{in} &= z_{rotor} \end{aligned} \tag{13}$$

The gravitational potential energy of the inner ring and the rotor is listed as

$$V_{in} = m_{in} g y_{in} \tag{14}$$

$$V_{rotor} = m_{rotor} g y_{rotor} \tag{15}$$

2.3. Elastic Potential Energy Due to Contact between Roller and Raceway

Taking the *i*th roller as an example, the elastic potential energy comes from the contact deformation between it and the raceway. The magnitude of the load in the contact region is equal to the integral of the pressure in each element, which pressure is the product of the stiffness and the deformation [22]. So the load between the *i*th roller and the inner ring is computed as follows

$$\int_0^{\delta_{in}} K_e \delta^n d\delta = \frac{1}{n+1} K_e \delta_{in}^{n+1} = \frac{1}{n+1} K_{in} \delta_{in}^2 \tag{16}$$

where K_e—equivalent stiffness coefficient, N/mm;

n—load-deformation exponent;

K_{in}—contact stiffness between the *i*th roller and the inner ring, N/mm, which is defined as

$$K_{in} = K_e \delta_{in}^{n-1} \tag{17}$$

δ_{in}—deformation between the *i*th roller and the inner ring, mm.

Figure 3 shows that the distance between the *i*th roller and the inner ring is always varying due to the rotation of the outer roller and inner ring. The difference between the current distance and the initial distance is the contact deformation. If the deformation is lower than or equal to 0, contact does not occur; otherwise, the *i*th roller is in contact status. On the basis of the above analysis, the contact deformation is written as follows

$$\delta_{in} = R_i + R_{in} - \chi_i - \frac{u}{2} - H_{in} \tag{18}$$

where, R_i—the radius of the *i*th roller, mm;

R_{in}—the radius of the inner ring, mm;

χ_i—the current distance between the *i*th roller and the inner ring, mm;

u—radial clearance, mm;

H_{in}—the lubrication film between the *i*th roller and the inner ring, mm.

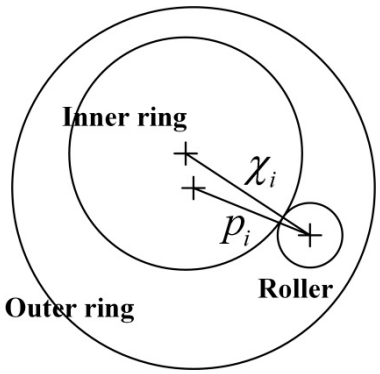

Figure 3. The relative positions of the *i*th roller and the inner ring with the inner ring rotating.

Figure 3 also reveals that the sum of the inner-ring displacement and the distance between the ith roller and the inner ring equals that of the outer-ring center and the *i*th roller, which can be decomposed in the X, Y, and Z directions and expressed as

$$x_{in} + \chi_i \cos(\phi_\chi) \cos(\alpha_i) = x_{out} + p_i \cos(\phi_i) \cos(\alpha_i) \tag{19}$$

$$y_{in} + \chi_i \sin(\phi_\chi) \cos(\alpha_i) = y_{out} + p_i \sin(\phi_i) \cos(\alpha_i) \tag{20}$$

$$z_{in} + \chi_i \sin(\alpha_i) = z_{out} + p_i \sin(\alpha_i) \tag{21}$$

The current distance, namely the real-time distance between the *i*th roller and the inner ring, can be solved as follows

$$\chi_i = \begin{pmatrix} x_{in}^2 + y_{in}^2 + z_{in}^2 + p_i^2 - 2x_{in}p_i \cos(\phi_i) \cos(\alpha_i) \\ -2y_{in}p_i \sin(\phi_i) \cos(\alpha_i) \pm 2z_{in}p_i \sin(\alpha_i) \end{pmatrix}^{1/2} \tag{22}$$

It is noted that the power of 1/2 is obtained by the formula derivation of Equations (19)–(21), namely the arithmetic square root.

α_i is contact angle and is defined as

$$\alpha_i = \alpha 0 + \alpha_{SAC} \tag{23}$$

where $\alpha 0$—initial contact angle, deg;

α_{SAC}—SRBs' self-aligning contact angle, deg.

In Equation (22), "±" represents different SRB rows. For instance, the symbol "+" means the right-row rollers are compressed if the direction of the external load is along with that of the Z axis. At this time, the left-row rollers are released, and "−" is used to represent them.

The analysis process of the outer ring is similar to that of the inner ring. The load in the contact region is written as

$$\int_0^{\delta out} K_e \delta^n d\delta = \frac{1}{n+1} K_e \delta_{out}^{n+1} = \frac{1}{n+1} K_{out} \delta_{out}^2 \tag{24}$$

where K_{out}—the contact stiffness, N/mm, which is defined as

$$K_{out} = K_e \delta_{out}^{n-1} \tag{25}$$

In Equation (24), δ_{out} is the elastic deformation between the *i*th roller and the outer ring. Taking Equation (18) as a reference, the deformation that occurs in the outer ring is determined as

$$\delta_{out} = p_i + R_i - R_{out} - \frac{u}{2} - H_{out} \tag{26}$$

H_{out} is the lubrication film between the *i*th roller and the outer ring. To sum up, the equation of total elastic potential energy is concluded as follows

$$V_{spring} = \frac{1}{n+1} \left(K_{in} \delta_{in}^2 + K_{out} \delta_{out}^2 \right) \tag{27}$$

2.4. Equivalent Stiffness Coefficient Taking the Consideration of UCS Condition

Undetermined contact status (UCS) is derived from the non-uniform contact regions between SRBs' rollers and the raceway, namely point-contact and line-contact conditions that exist simultaneously. In order to solve the problem, the contact region should be meshed so as to characterize it in detail. Generally speaking, the contact region is regarded as a plane since it just has a tiny deformation when loaded. Each contact region has its own local coordinate, and these local coordinates are isolated from each other. Taking the *i*th roller for example, the directions X_i and Y_i are defined as the parallel and perpendicular directions of the rollers rotation; meanwhile, the direction Z_i is perpendicular to $X_iO_iY_i$ plane, which is marked in Figure 4. According to non-classical Hertzian contact theory, the

distance equals the product of the flexibility coefficient times force, where force is equal to the integral of the pressure in the elements [22]. The relevant equation is

$$\omega(x,y) = \frac{1-\upsilon^2}{\pi E} \times \iint_{S_c} \frac{p(x',y')dx'dy'}{\sqrt{(x-x')^2+(y-y')^2}} \tag{28}$$

where ω—initial distance between the contact surfaces of an element in the contact region, mm;

(x,y), (x',y')—coordinate of an element;

υ—Poisson's ratio;

E—elasticity modulus, MPa;

S_c—the range of the contact region;

p—the pressure of an element, MPa.

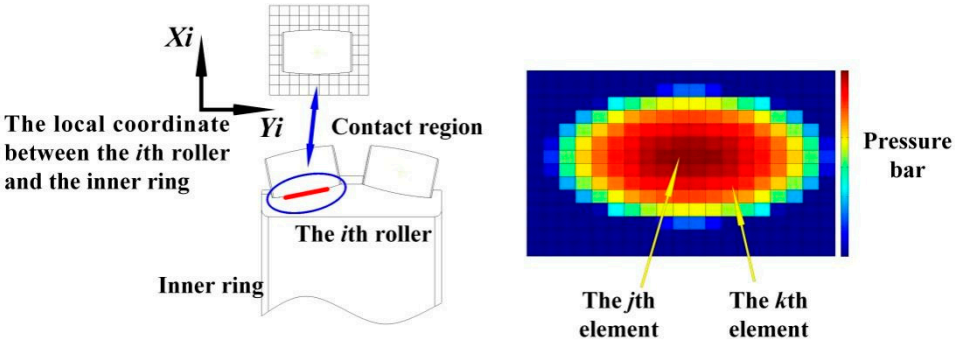

Figure 4. The contact region between the *i*th roller and the inner ring.

Assuming that the contact region is divided into elements, whose length and width are a and b, respectively. When the contact occurs for the *i*th roller, the deformation is caused by the deformation in the *j*th element as well as the adjacent element, for instance, the *k*th element. To put it another way, any element in the contact region has an effect on the *j*th element. Besides, if the quality of the meshing is perfect, the pressure in each element is considered a constant. In light of the above analysis, Equation (28) can be rewritten as

$$\omega_{jk} = \frac{(1-\upsilon^2)}{\pi E} \times p_k \times \int_{x_k-a_k}^{x_k+a_k} \int_{y_k-b_k}^{y_k+b_k} \frac{dx'dy'}{\sqrt{(x_j-x_k-x')^2+(y_j-y_k-y')^2}} \tag{29}$$

The formula used to establish the relationship between the *j*th and *k*th elements is called the flexibility coefficient, which is listed as follows

$$FC_{jk} = \frac{(1-\upsilon^2)}{\pi E} \times \int_{x_k-a_k}^{x_k+a_k} \int_{y_k-b_k}^{y_k+b_k} \frac{dx'dy'}{\sqrt{(x_j-x_k-x')^2+(y_j-y_k-y')^2}} \tag{30}$$

On the basis of non-classical Hertzian contact theory, the relationship between the external load and the deformation is defined as

$$\begin{cases} F = \iint_{S_c} p(x',y')dx'dy' \\ \delta - \omega(x,y) == \frac{1-\upsilon^2}{\pi E} \times \iint_{S_c} \frac{p(x',y')dx'dy'}{\sqrt{(x-x')^2+(y-y')^2}} \end{cases} \tag{31}$$

where, F—external load, which is given as a known condition, kN;

δ—deformation between the roller and the raceway, mm;

So SRBs' stiffness coefficient is computed as follows

$$K_{SRBs} = F/\delta \tag{32}$$

2.5. Determination of the Self-Aligning Contact Angle (SAC Angle)

There are two kinds of contact angles, namely the initial contact angle and the SRB's self-aligning contact angle (SAC angle). For the former, the value is a constant due to the geometrical structure, but for the latter, its magnitude and direction are obtained in light of the rotor bending since there is no constraint between the inner and outer rings. Besides, the SAC angle is different for each roller in different positions.

The magnitude of the SAC angle is evaluated by the rotor's bending based on the Finite Element Method (short for FEM). The stiffness matrix of a beam element [23] shown in Figure 5 is written as below.

$$K_{rotor-i} = \frac{EI_{rotor-i}}{l^3}\begin{bmatrix} 12 & 6l & -12 & 6l \\ 6l & 4l^2 & -6l & 2l^2 \\ -12 & -6l & 12 & -6l \\ 6l & 2l^2 & -6l & 4l^2 \end{bmatrix} \tag{33}$$

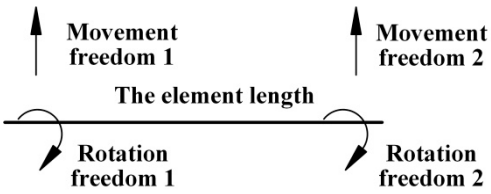

Figure 5. Any element in a rotor.

In Equation (33), $K_{rotor-i}$—the stiffness of the ith beam element, N/mm;
E—the elastic modulus of the rotor, MPa;
$I_{rotor-i}$—the inertia moment of the ith beam element, mm^4, which is expressed as

$$I_{rotor-i} = \frac{\pi D_{rotor}^4}{64} \tag{34}$$

l—the length of the ith beam element, mm;
D_{rotor}—the diameter of the rotor cross-section, mm.

The comprehensive stiffness of the SRBs-rotor system is equal to the linear superposition of the bearing stiffness and rotor stiffness. The position of the bearing superposition is located on the node, which represents the bearing pedestal on the rotor. The reason for this is that the bearing and the rotor are in a parallel relationship and are both supporting the external load.

The deformation of each node equals the external load times the reciprocal of the SRBs-rotor system stiffness. At this moment, the angular misalignment between the inner and outer rings, namely the SAC angle, is evaluated in light of rotor bending.

The SAC angle is constant if the external load is unchanged. On the contrary, it will change as the load varies over time. So for each time step, it is necessary to check the magnitude of the SAC angle, especially for the dynamic loading.

What is more, each roller has its own SAC angle since their position angles are different from each other. As shown in Figure 6, there are two forms of roller distribution: staggered and parallel. According to SRBs' geometrical structure, the position angle of the ith roller in misaligned form is defined as

$$\phi_{i-left} = \frac{2\pi}{Z} \times (i-1) \tag{35}$$

$$\phi_{i-right} = \frac{2\pi}{Z} \times (i-1) + \frac{\pi}{Z} \tag{36}$$

The corner marks "*left*" and "*right*" mean the left and right rows, respectively.

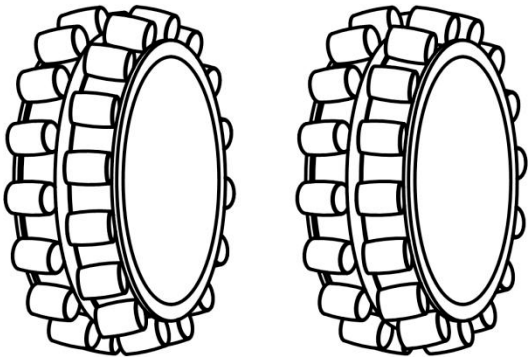

Figure 6. Forms of rollers distribution, staggered and parallel.

The SAC angle for each roller will vary with position; however, its magnitude can be calculated according to the roller's position.

$$\alpha_{SAC-left} = \left(1 - \frac{\phi_{i-left}}{90}\right) \times \alpha_{SAC} \tag{37}$$

$$\alpha_{SAC-right} = -\left(1 - \frac{\phi_{i-left}}{90}\right) \times \alpha_{SAC} \tag{38}$$

2.6. The Coupling of the Lubrication Film

Elastic-hydrodynamic lubrication (EHL) is often used to characterize the influence of the lubrication medium, including oil or grease, whose key point is to solve Reynolds' equation. However, because the computing amount of the EHL procedure is large and nearly impossible to calculate in each time step, it is difficult to realize in dynamic equations.

In order to solve the above problem based on the classical EHL procedure, the average thickness and the minimum thickness of the lubrication film are computed with different parameters [24], such as load, rotational speed, material, and so on. Then, two arrays, namely the film between the roller and the inner or outer ring, are established to be databases with the above five parameters. When the Lagrange equation is calculated, the film thickness can be directly obtained in the databases according to the parameters of load, rotational speed, and material. If the relevant film thickness is not found in the database, the interpolation method is used to find a proper solution. We called it the look-up table method.

The computing method of the EHL procedure is perfect, so it no longer needs to be repeated. A loop-up table has the advantage of conserving computing resources. On the other hand, the loads applied to different rollers are varying due to different position angles, so the film thickness between each roller and the raceway is changing with the time step, which can also be fully characterized.

In this paper, the lubrication medium is regarded as a spring-damping system that is used to modify contact stiffness and damping between the *i*th roller and the raceway in each time step, respectively.

Assuming that the elastic deformation of the lubrication medium equals the film thickness, the lubrication medium stiffness is obtained as

$$K_c = \frac{Q}{H_c} \tag{39}$$

where K_c—the stiffness of the lubrication medium, N/mm;

Q—the contact force between the roller and the raceway in the *i*th time step, N;

H_c—film thickness, mm.

In view of the series connection between the roller and the inner or outer ring, the modified stiffness can be defined as

$$K_{in-hc} = \frac{1}{\frac{1}{K_{in}} + \frac{1}{K_{c-in}}} \tag{40}$$

$$K_{out-hc} = \frac{1}{\frac{1}{K_{out}} + \frac{1}{K_{c-out}}} \tag{41}$$

where K_{in-hc} and K_{out-hc} are the modified stiffness of the inner and outer rings, respectively. Similarly, an SRB's comprehensive stiffness after being modified is given as

$$K_e = \frac{1}{\frac{1}{K_{in-hc}} + \frac{1}{K_{out-hc}}} \tag{42}$$

In light of Tandon's explanation [25], the damping between the roller and the raceway is expressed as below

$$C_r = 8\frac{\xi {a_h}^3 L \tau_c}{{H_{\min}}^3} \tag{43}$$

where C_r—damping coefficient, N/(m/s);

ξ—absolute viscosity, Pa.s;

a_h—a computing parameter, which equals

$$a_h = 1.52\left(\frac{QR}{L}E\right)^{0.5} \tag{44}$$

L—the length of the ith roller, mm;

R—the radius of the ith roller, mm;

E—the elastic modulus of the ith roller, MPa;

τ_c—edged factor, which is defined as

$$\tau_c = 1 - 1.2\frac{a_h}{L} \tag{45}$$

H_{min}—the minimum film thickness, mm.

Taking the modified method of the SRB's comprehensive stiffness as an example, the modified damping of the ith roller is shown as follows

$$C_i = \frac{1}{\frac{1}{C_{i-in}} + \frac{1}{C_{i-out}}} \tag{46}$$

where C_i—the damping of the ith roller, N/(m/s);

C_{i-in}—the damping between the ith roller and the inner ring, N/(m/s);

C_{i-out}—the damping between the ith roller and the outer ring, N/(m/s).

The comprehensive damping is equal to the sum of the entire rollers' modified damping.

$$C_{tot} = \sum_{row=1}^{2}\sum_{i=1}^{N}(C_i \times \cos(\phi_i)) \tag{47}$$

2.7. SRBs Dynamic Equation

On the basis of the above analysis, a comprehensive SRBs dynamic model is summarized. It is assumed each roller has one freedom, namely the displacement in the normal direction, and the expression is obtained as below

$$m_i\ddot{p}_i + C_{tot}\dot{p}_i - m_i\left(\cos(\alpha_i)\dot{\phi}_i\right)^2 p_i + m_i g\cos(\alpha_i)\sin(\phi_i) + K_e\delta_{in}^n\left(-\frac{\partial\chi_i}{\partial p_i}\right) + K_e\delta_{out}^n = F_i \tag{48}$$

The displacements in X, Y, and Z directions are the freedoms belonging to the inner ring or rotor, and the relevant dynamic equations are derived as

$$\begin{cases} (m_{in}+m_{rotor})\ddot{X}_{in}+C_{tot}\dot{X}_{in}+K_e\left(\sum\limits_{row=1}^{2}\sum\limits_{i=1}^{Z}\left(\delta_{in}^{n}\times\left(-\frac{\partial\chi_i}{\partial X_{in}}\right)\right)\right)=F_x \\ (m_{in}+m_{rotor})\ddot{Y}_{in}+C_{tot}\dot{Y}_{in}+(m_{in}+m_{rotor})g+K_e\left(\sum\limits_{row=1}^{2}\sum\limits_{i=1}^{Z}\left(\delta_{in}^{n}\times\left(-\frac{\partial\chi_i}{\partial Y_{in}}\right)\right)\right)=F_y \\ (m_{in}+m_{rotor})\ddot{Z}_{in}+C_{tot}\dot{Z}_{in}+K_e\left(\sum\limits_{row=1}^{2}\sum\limits_{i=1}^{Z}\left(\delta_{in}^{n}\left(-\frac{\partial\chi_i}{\partial Z_{in}}\right)\right)\right)=F_z \end{cases} \quad (49)$$

These dynamic equations can be solved by the Runge-Kutta method.

3. Experimental Facility and Testing Method

3.1. General Layout of the Test Rig

A test rig is established, as shown in Figure 7. The rotor is supported by two sliding bearings. The authors created a novel SRB pedestal with a self-aligning function. Loading equipment is connected to the SRB's pedestal via a ring on the pedestal's shell, whereby the radial force can be applied and obtained. The vibration signal is captured by the displacement sensors arranged in horizontal and vertical directions. The relevant data is processed and saved in real time.

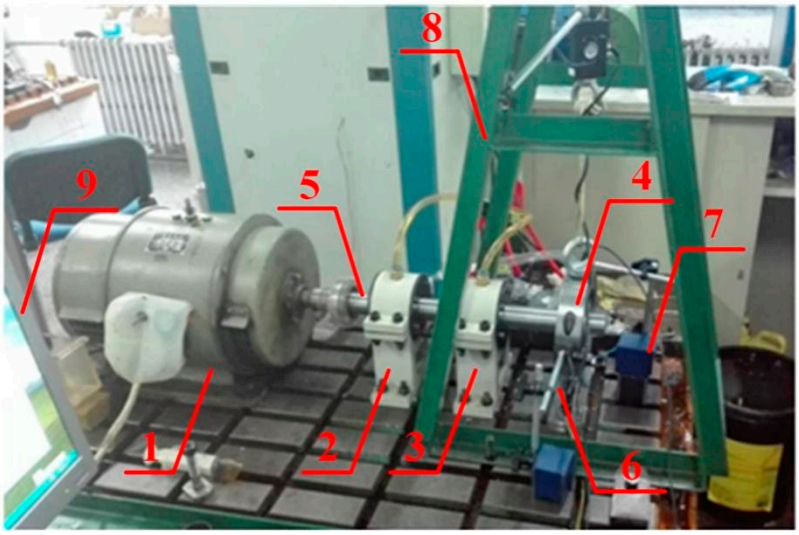

Figure 7. Test rig. 1 electrical machine; 2–3 sliding bearings for supporting; 4 SRBs pedestal with self-aligning function; 5 rotor; 6–7 displacement sensors; 8 loading equipment; 9 computer.

3.2. A Novel SRBs Pedestal with Self-Aligning Function

Figure 8 shows a novel SRB pedestal with a self-aligning function. The inner-ring fixture is rigidly joined to both the rotor and the testing bearing. The outer-ring fixture is not only joined to the SRB's outer ring but also connected to the mass disc via the loading ring. As shown in Figure 8d, the locating pin is driven by the limiting bolt adjusting; meanwhile, the locating pin is also rigidly jointed with the outer-ring fixture, thereby allowing the outer-ring fixture to freely rotate relative to the inner-ring fixture by the adjusting of the limiting bolt, namely realizing SRBs' self-aligning operating condition. A gap of 2 mm is reserved between the locating pin and the foundation so as to avoid the friction in Figure 8e. The swing range of the limiting bolt is smaller than 4 degrees, which is the extremity of the self-aligning contact angle in the SRB's instruction manual, whereby the processes of the self-aligning experiment are safe and under control. In addition, an adjusting bolt is used to restrict the position of the limiting bolt, so the latter can be self-aligning with any angles in the safety range. When disassembling the adjusting bolt, which means canceling the restriction for the limiting bolt, the outer ring is under the self-adjusting condition.

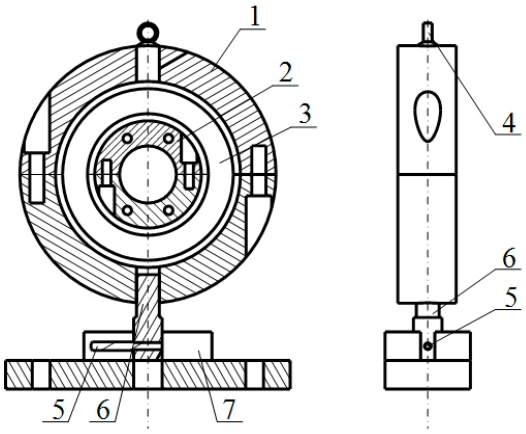

(**a**) Schematic of SRBs pedestal

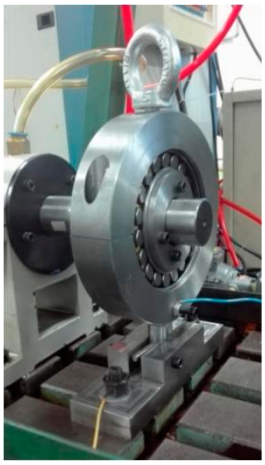

(**b**) Assembly

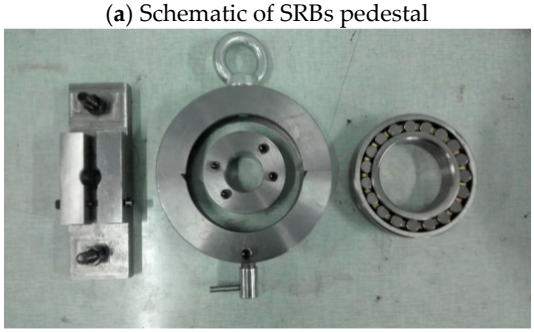

(**c**) Parts

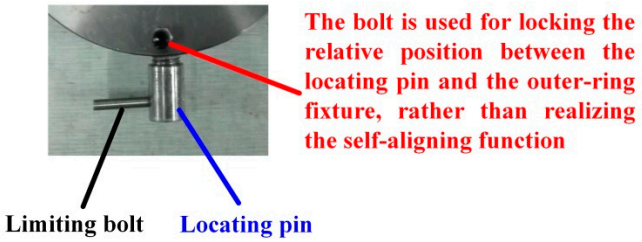

(**d**) Explanation of self-aligning function

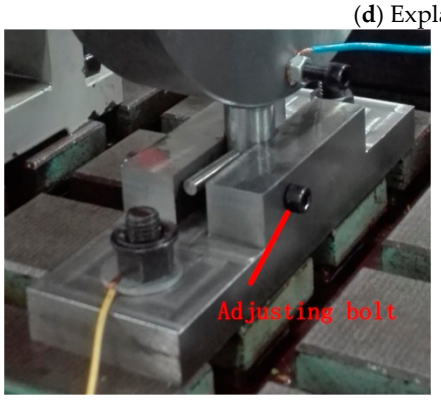

(**e**) Foundation with restricting function

Figure 8. SRBs pedestal with self-aligning function. 1 outer-ring fixture; 2 inner-ring fixture; 3 SRB under test; 4 loading ring; 5 limiting bolt; 6 locating pin; 7 foundation; 8 adjusting bolt.

3.3. Testing Bearings and Operating Condition

Five types of testing bearings are shown in Figure 9, all of which are SRBs with the 22215 product type. In light of the fact that these SRBs are produced by different manufacturers, they have different geometric structures, which are not listed in detail.

In this experiment, two operating conditions will be set. Under the first, no constraint is imposed on the outer ring except for an external load applied in the radial direction only via the loading ring. In this case, the inner and outer rings will realize that self-aligning behavior depends completely on the SRB's spherical structure itself, which is defined as an adaptive self-aligning operating condition. This condition simulates the classical status of the rotor of the wind power equipment, which is that the main rotor will bend in any direction with wind power, wind direction, wind speed, and so on.

Under the other one, the angular misalignment between the inner and outer rings is constant and exists, which is realized by limiting the position of the outer-ring fixture via the limiting bolt in Figure 8e. Namely, an external load from the limiting bolt ensures a

constant self-aligning contact angle, which is named the limiting self-aligning operating condition. This condition simulates the rotor being bent by an extremely large force in a constant direction.

Figure 9. SRBs with different brands.

3.4. Testing System

A real-time testing system is designed to obtain signals of displacement and tension. Two capacitive displacement sensors (Micro-Epsilon capaNCDT6100) are arranged near the SRB's pedestal in horizontal and vertical directions. The range of the tension sensor is 200 kN, meeting the requirement of the test. The sensors are shown in Figure 10 and convert the physical signals into electrical signals. The basic parameters of the data acquisition card (PCI8622, shown in Figure 11) are 32 channels, 16-bit resolution, and 250 KS/s sampling frequency. Self-written data-processing software is shown in Figure 12 and realizes the functions of data management, real-time display, storage, and so on.

(**a**) Capacitive displacement sensor

(**b**) Tension sensor

Figure 10. Sensors.

(**a**) Acquisition system

(**b**) Data acquisition card PCI8622

Figure 11. Data acquisition system.

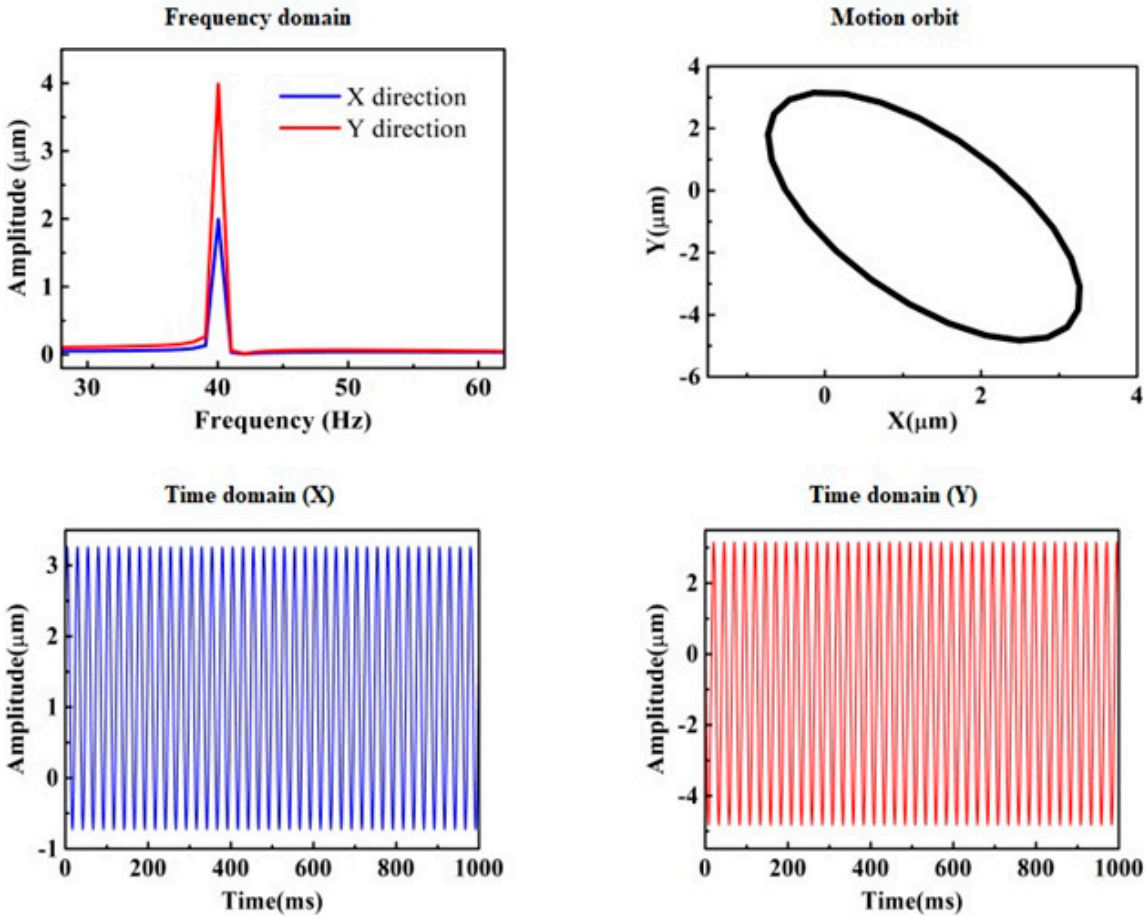

Figure 12. A data-processing software programmed by the authors.

4. Results and Discussion

4.1. Theoretical Verification

In Section 4.1, SRBs' dynamic characteristics are simulated and compared with the published results under the non-self-aligning operating condition, which will verify the correctness and rationality of the model proposed in this paper. SRBs' material and geometrical parameters are listed in Table 1, and the global coordinate is referred to in Figure 2. The external loads in the X, Y, and Z directions are 12 kN, 18 kN, and 0.15 kN, respectively. And a random load ranging from 1~50 N is also existed. In addition, the rotor speed is 1200 rpm. A set of SRBs' fundamental geometrical and material parameters are listed in Table 1. It should be noted that some parameters may not be the same with different SRB brands.

Table 1. SRBs' fundamental geometrical and material parameters.

Name	Symbol	Value	Unit
Roller's circumferential radius	R_{i-x}	14.5	mm
Roller's axial radius	R_{i-y}	103.95	mm
Roller's effective length	$L_{eff-roller}$	20.762	mm
SRB pitch diameter	D_p	175	mm
Axial radius of the inner-ring raceway	$R_{in-rw-y}$	106.61	mm
Axial radius of the outer-ring raceway	$R_{out-rw-y}$	106.61	mm
Initial contact angle	$\alpha 0$	7.92	deg
Radial clearance	u	0.041	mm
Elastic modulus	E	206	GPa
Poisson's ratio	v	0.3	—

Figure 13a depicts the steady-state motion orbit of the SRB, which is a closed circle. To be specific, it is not a regular circle but a long and narrow one. The reason for this is that the bearing is subjected to external loads in both directions. The shape of the SRB's motion orbit is also influenced by the axial load, which leads to unbalanced loading to a certain degree.

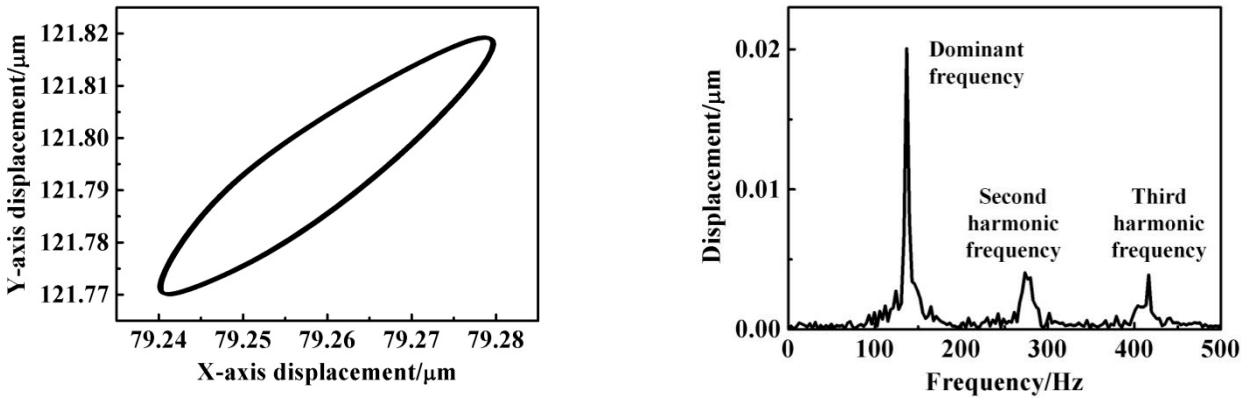

(**a**) Motion orbit (**b**) The frequency spectrum of displacement in Y direction

Figure 13. Dynamic characteristics of the inner ring.

Taking the displacement spectrum of the inner ring in the Y direction as an example, shown in Figure 13b, the dominant frequency (and its multiples) is approximately equal to the passing frequency (or its integer multiples) of a roller [26]. Namely the times of the roller passing through a certain point of the outer-ring raceway per unit-time. The relevant formula is defined as

$$f = m \times Z \times f_r \tag{50}$$

where f—dominant frequency, Hz;

m—integer;

Z—the number of rollers in one row;

f_r—the revolution frequency of the rollers, Hz.

The conclusion is in agreement with that in the published references [27,28].

Figure 14a,b highlights that the normal displacement of the roller changes regularly during its revolution period. When the roller enters the loading region, its normal displacement increases gradually and then decreases, which means the loading mission begins from secondary loading to primary loading and then to secondary loading. On the contrary, the roller displacement oscillates slightly in the non-loading region.

Figure 14c,d show the changing law of the velocity is similar to that of the displacement, namely, increasing gradually and then decreasing. Moreover, the amplitude of the roller has an obvious oscillation at the moment of leaving the loading region due to the inertia force but is restored immediately. The dominant frequency of the normal displacement equals the revolution frequency (or its integer multiples) of all the rollers, shown in Figure 14e, which is the same as Cao's conclusion [2].

In light of the above analyses, there is no obvious difference between SRBs and other kinds of bearings under the non-self-aligning operating condition, which proves the correctness of the proposed model in this paper. On the other hand, it also illustrates that it is necessary to analyze SRB's dynamic characteristics under the self-aligning condition.

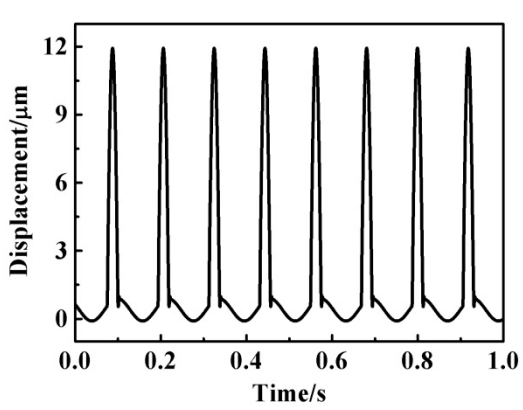

(**a**) The time domain of the normal displacement

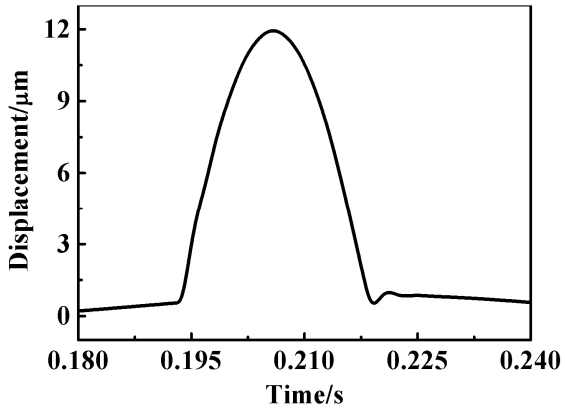

(**b**) Normal displacement in one period

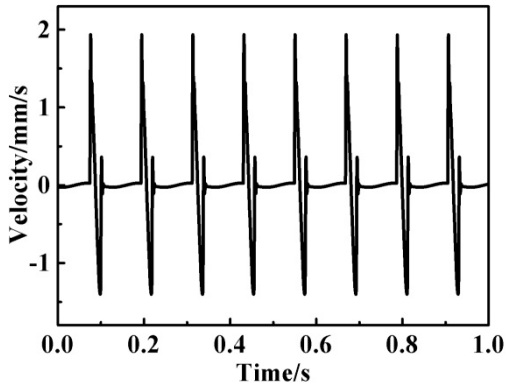

(**c**) The time domain of the normal speed

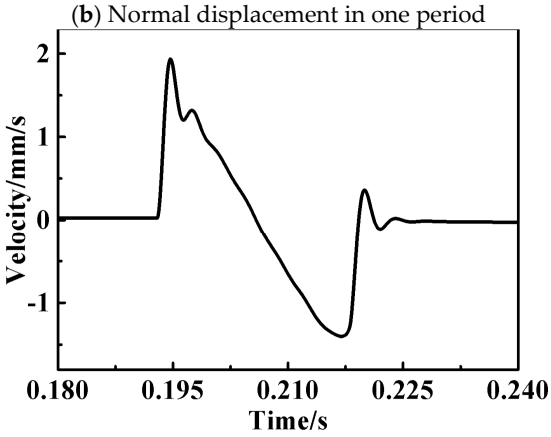

(**d**) Normal speed in one period

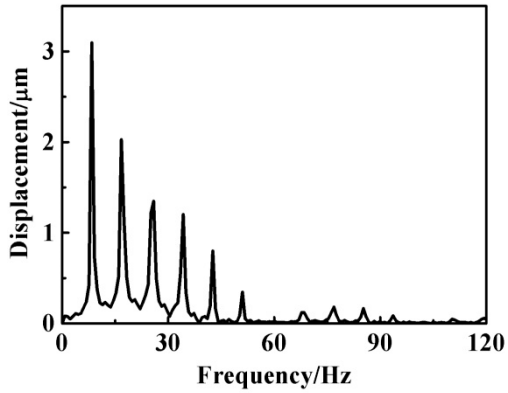

(**e**) The frequency domain of the normal displacement

Figure 14. The service performances of the rollers.

4.2. The Dynamic Characteristics of Each SRBs Component under the Self-Aligning Operating Condition

SRBs' self-aligning function is their most important feature, which makes them different from other rolling bearings. The dynamic characteristics of the inner ring and the roller under the self-aligning operating condition will be researched in this section. According to the SKF bearing manual, the range of the SAC angle is generally about 0~2.5 degrees. To investigate the performance of SRBs under extreme conditions, the SAC angle is assumed to be 0~4 degrees. Other parameters are the same as before.

Figure 15 shows how the motion orbit of the inner ring varies with different SAC angles. The motion orbit is distorted by degrees if the SAC angle is positive, indicating that the inner ring is rotating clockwise relative to the outer ring. The larger the SAC angle is,

the more obvious the distortion is. On the contrary, when the SAC angle is negative, the motion orbit is stretched.

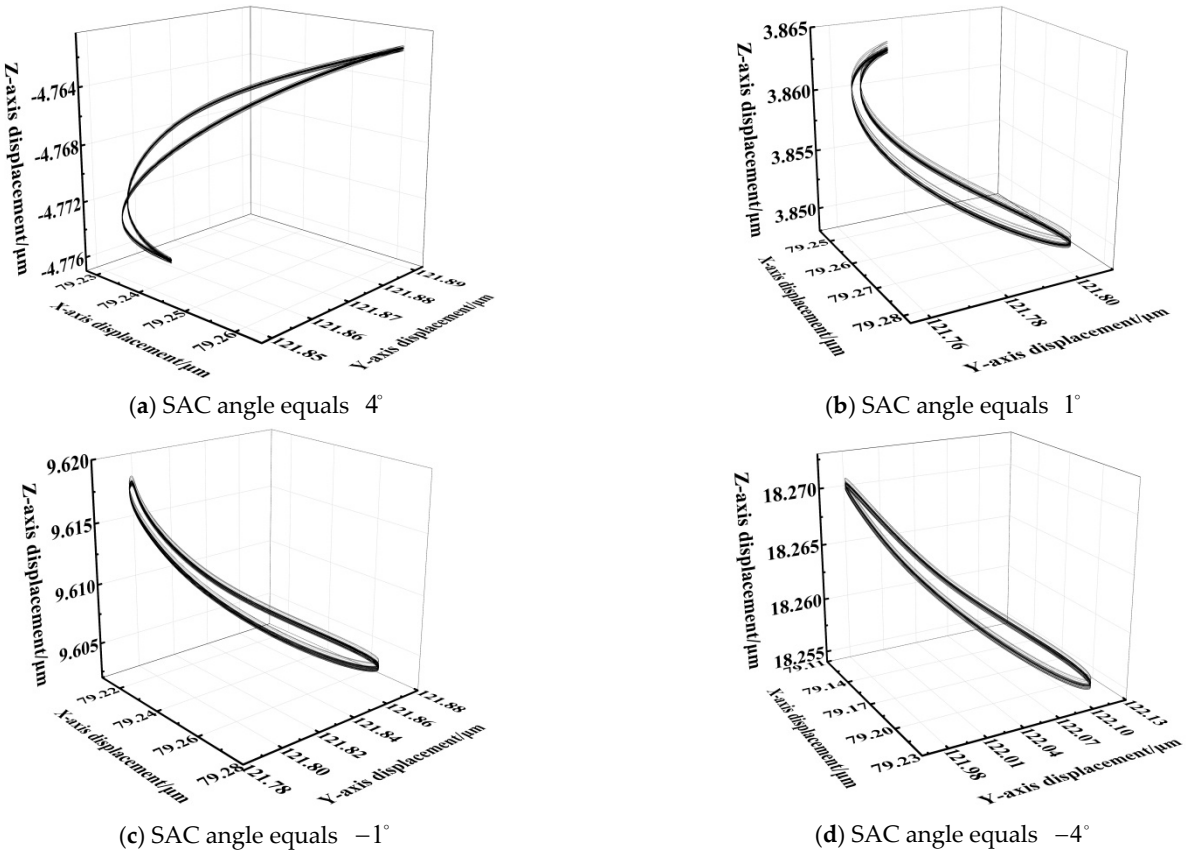

(**a**) SAC angle equals 4°

(**b**) SAC angle equals 1°

(**c**) SAC angle equals -1°

(**d**) SAC angle equals -4°

Figure 15. The motion orbit of the inner ring with different self-aligning contact angles (SAC angles).

The reason lies in the fact that the axial load will lead to the unbalanced loading of two-row rollers. For instance, if the direction of an axial load is applied to SRBs from left to right, the rollers in the right row will be compressed while the left rollers will be released. At the moment, the phenomenon of unbalanced loading is improved with the SAC angle rotating anticlockwise. Specifically, more rollers in the left row will enter the loading region to share the external load with the rollers in the right row. The load distribution among all the rollers becomes more reasonable, and the motion orbit of the inner ring seems stretched and smooth.

It has been proven that the negative SAC angle is better than the positive one to ensure the motion orbit is steady with an axial load from left to right. Hence, for the former, a larger magnitude is beneficial for balancing the loads of two-row rollers. By the same token, a positive SAC angle with a smaller magnitude can reduce the effect of the unbalanced loading as much as possible.

Additionally, the radius of the motion orbit is approximately equal, which proves the amplitude of the inner ring is determined by the external load, but the shape is influenced by the direction and magnitude of the SAC angle.

The frequency of the inner ring shown in Figure 16 is more complicated than the frequency in Figure 13b. Some additional frequencies are obviously aroused, especially around the frequency that the roller is passing one point of the outer-ring raceway (about 136.8 Hz). The additional frequency equals 8.3 Hz (namely the revolution frequency of all the rollers) or its integer multiples, approximately. All the frequencies in Figure 16, including the dominant frequency and the additional frequency, can be expressed by the following equation

$$f = m \times Z \times f_r \pm n \times f_r \tag{51}$$

where f—the dominant frequency or the additional frequency, Hz;

m—an integer used to characterize the multiple of the dominant frequency;

n—an integer used to characterize the multiple of the revolution frequency of all the rollers;

f_r—the revolution frequency of all the rollers, Hz.

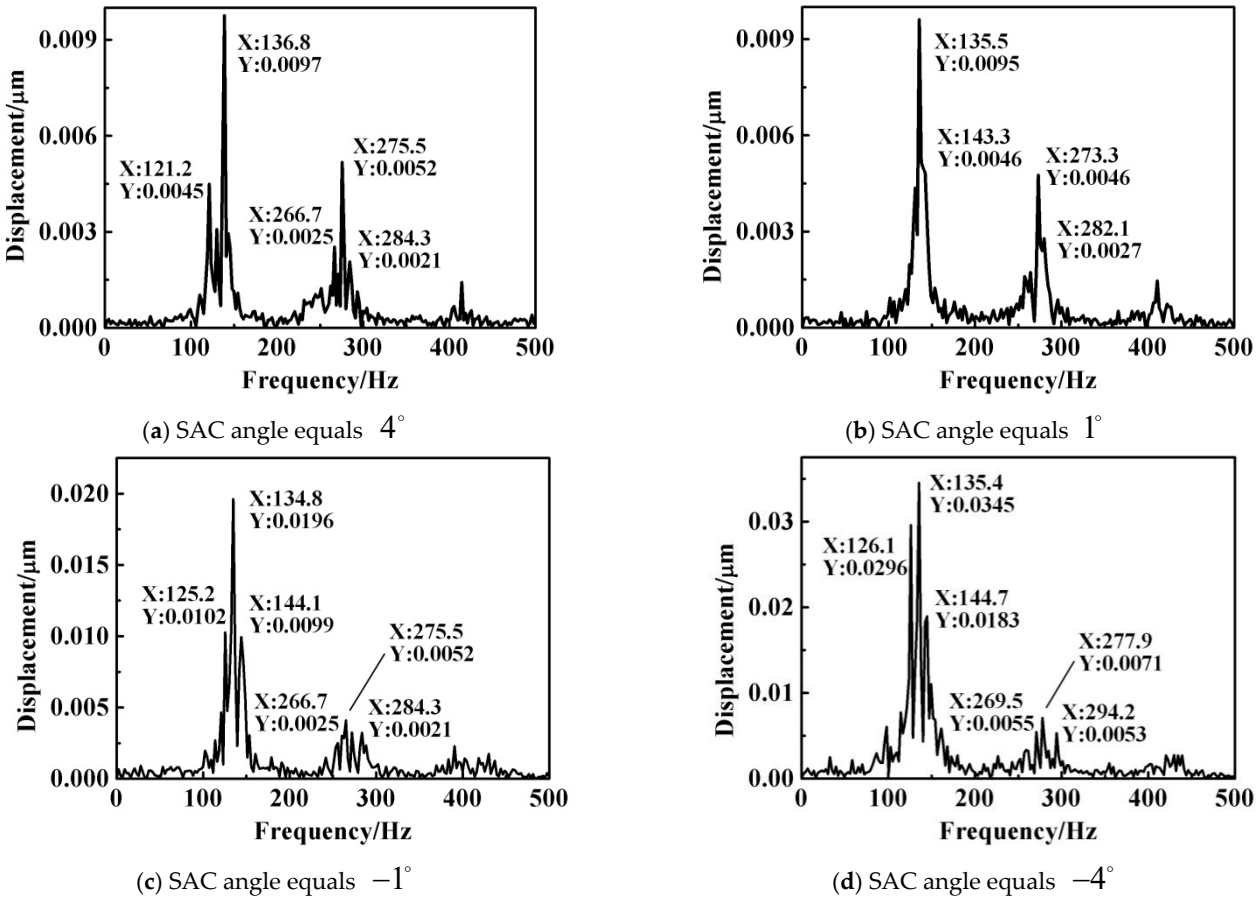

(**a**) SAC angle equals 4°

(**b**) SAC angle equals 1°

(**c**) SAC angle equals -1°

(**d**) SAC angle equals -4°

Figure 16. The displacement spectrum of the inner ring in Y direction with different SAC angles.

In view of the fact that the magnitude of the higher frequency is smaller, it is useless to give a larger value to m and n. In another word, the vibration features are better characterized by their smaller frequency since they have a larger amplitude. As a result, the recommended range for m and n in Equation (51) is less than 5.

The motion orbits in Figure 15 have different performances with varying SAC angles, despite the additional frequencies that exist in each frequency spectrum in Figure 16. It indicates again that SRBs' service performance could be improved by a proper direction of the SAC angle. For example, the motion orbit is steady when the direction of the axial load is along with the Z direction and the SAC angle is negative. Conversely, the motion orbit of the inner ring will be distorted if the SAC angle is positive. Additionally, under the same operating condition, the additional frequency is becoming more and more obvious, namely the magnitude, which is increasing with the SAC angle from 4 degrees to -4 degrees. These factors will contribute to a steady rotation for the inner ring.

It should be noted that the influence derived from the self-aligning function is the result of a comprehensive set of constraints rather than one that reduces vibration complexity. So the direction and magnitude of the SAC angle are the key points to improving the SRB's dynamic characterization.

The dynamic characteristics of the inner ring are determined by the unbalanced loading of all the rollers due to the SRB's self-aligning function. So it is different for the amplitudes

of the rollers in the left and right rows, which show a characteristic of "one loss but the other gain", as illustrated in Figure 17a,b. Because of an axial load from left to right, the load on the SRBs roller in the right row is larger than that in the left row, whereby the normal vibration of the right-row roller has a larger span in the time domain. Correspondingly, the vibration speed of the right-row roller entering or leaving the loaded region is slightly greater than that of the left-row roller, as revealed in Figure 17c,d. Particularly in the entering or leaving period, the vibration speeds will oscillate slightly and then recover gradually for both the left and right rollers. The oscillating behavior is also the reason for some additional frequencies. It is noted that because of the staggered roller distribution, the two rollers in different rows do not enter the loaded region synchronously.

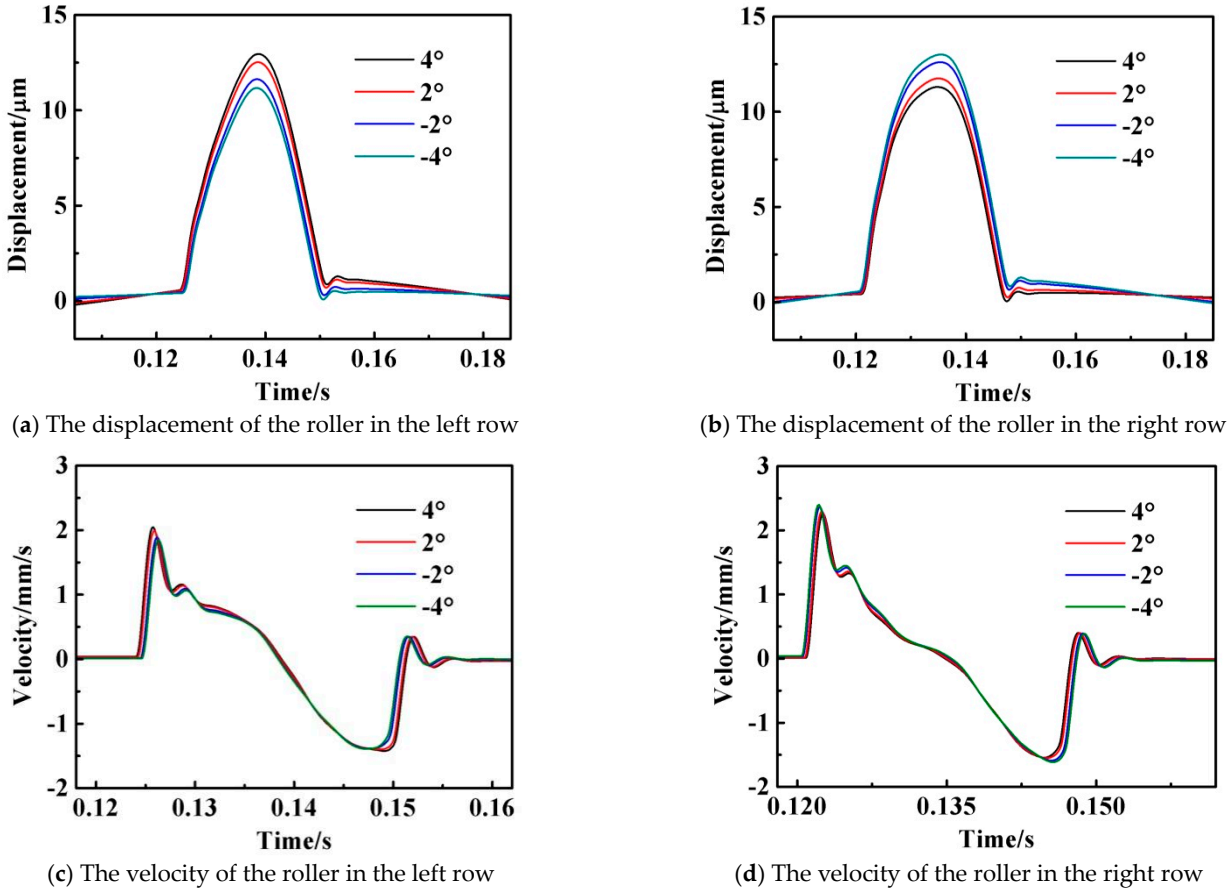

(**a**) The displacement of the roller in the left row

(**b**) The displacement of the roller in the right row

(**c**) The velocity of the roller in the left row

(**d**) The velocity of the roller in the right row

Figure 17. The motion orbit of a roller with varying SAC angles in a revolution period.

4.3. SRBs Dynamic Characterization under the Low-Speed and Heavy-Load Operating Condition

This section examines the dynamic characterization of SRBs with self-aligning functions under low-speed and heavy-load operating conditions. Referring to the bearing manual, it is assumed that the rotating speed is 1200 rpm and the external loads are 12 kN, 18 kN, and 0.15 kN in the X, Y, and Z directions, respectively. In light of the bearing manual, the maximum equivalent load and the rated speed of this type of bearing are 190 kN and 3400 rpm, respectively.

According to the empirical formula given in the bearing manual, the original load is approximately equal to a 22 kN equivalent dynamic load, while 5 times the original load is about 110 kN equivalent dynamic load. In general, the working load should be less than 60% of the equivalent dynamic load in order to withstand random loads and unexpected shocks. Therefore, 22 kN represents a light load, and 110 kN represents a heavy load.

Figure 18a indicates the motion orbit of the inner ring is steady with a light load despite the self-aligning operating condition. When the external load is increased to 5 times the original value, namely the heavy-load condition, the motion orbit is distorted and looks

like an "8" shape, as shown in Figure 18b. A steady orbit is derived from the constant value of the external load, but the larger magnitude and the unreasonable combination of the radial and axial loads contribute to a distorted motion orbit. Figure 18c shows that a proper axial load can improve SRBs' service performance, which is theoretically suitable for nearly all kinds of radial rolling bearings. In the case of Figure 18d, even if the SAC angle is close to the limit, a larger axial load improves the motion orbit of the inner ring significantly.

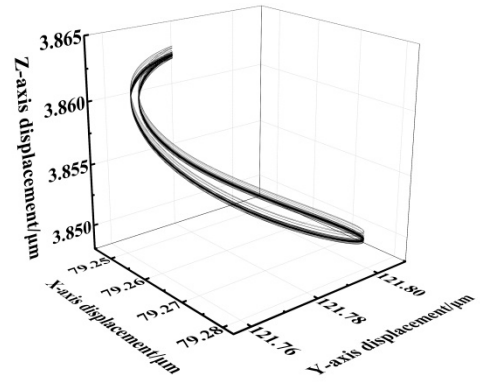

(**a**) Original loads*1, SAC angle 1°

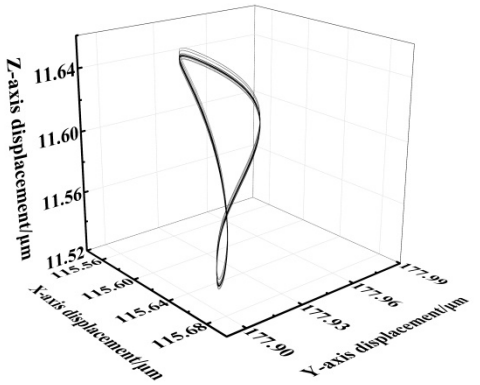

(**b**) Original loads*5, SAC angle 1°

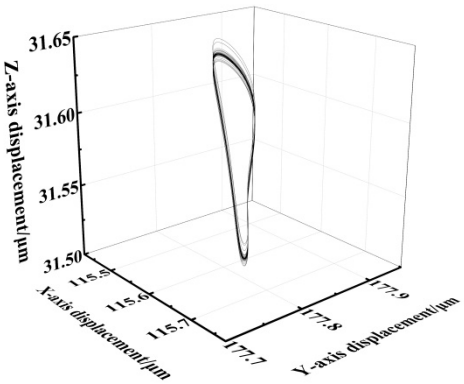

(**c**) Radial load*5; Axial load*10; SAC angle 1°

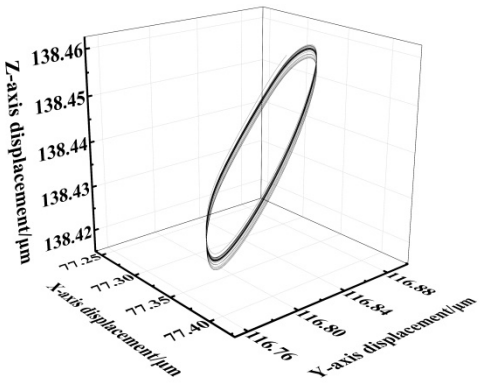

(**d**) Radial load*1; Axial load*20; SAC angle 3°

Figure 18. The motion orbit of the inner ring with a rotating speed of 1200 rpm under the heavy-load and self-aligning operating conditions.

In Figure 18d, despite the fact that the vibration is suppressed by the axial load, the SRBs' rollers are under the unbalanced loading status, and the relevant amplitudes have a large difference, which is shown in Figure 19. It is extremely detrimental to bearing life, resulting in interference with SRB components, heating, and so on. So it is inadvisable to use SRBs to bear an axial load directly, except for an axial preload and an accidental random load of a small magnitude. Besides, it is not recommended to suppress the vibration by increasing the axial preload, too.

By comparing Figure 20a,b, it is clear that slowing down the rotation speed results in more stable service performance. Especially when the speed is reduced to 600 rpm, the motion orbit of the inner ring is closer to a circle, as shown in Figure 20c. If the speed goes up to 1600 rpm, which is basically half the allowable rotating speed, despite the fact that the SAC angle is smaller in Figure 20d, the motion orbit of the inner ring is severely distorted. At this moment, the motion orbit will be improved by increasing the axial preload, as shown, for instance, in Figure 20e. However, this measure will give rise to the unbalanced loading of the rollers in the left and right rows, as mentioned before. If SAC angle and axial preload could be combined in a proper way via adjusting the position of the inner or outer ring, it would not only obtain the similar motion orbit but also avoid unbalanced loading due to excessive axial preload to the greatest extent, which is illustrated in Figure 20f.

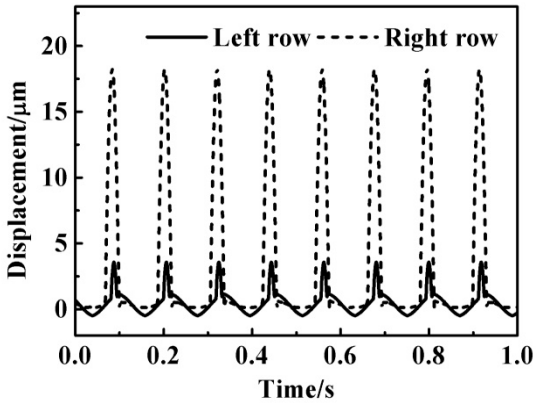

Figure 19. The normal displacements of two-row rollers under the same operating condition are shown in Figure 18d.

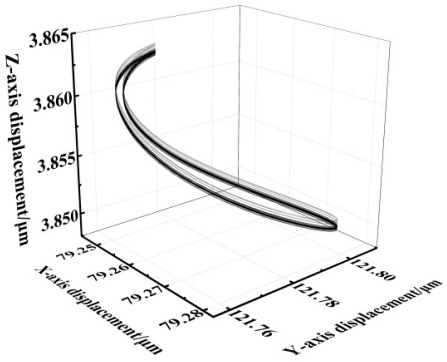

(**a**) Original load*1, 1200 rpm, SAC angle 1°

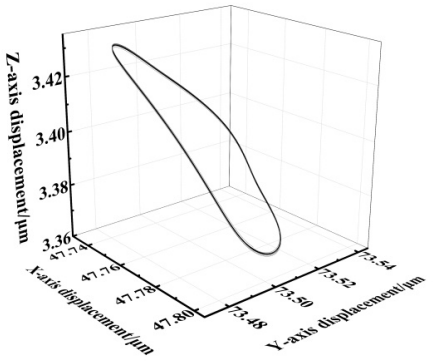

(**b**) Original load*1, 800 rpm, SAC angle 1°

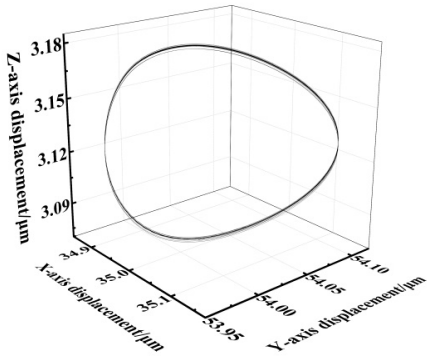

(**c**) Original load*1, 600 rpm, SAC angle 1°

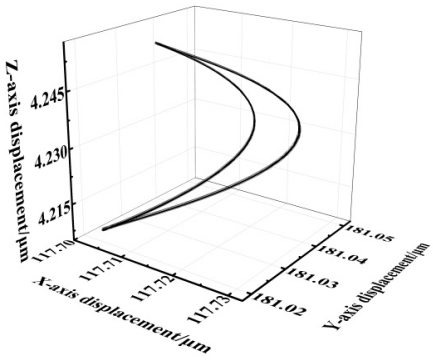

(**d**) Original load*1, 1600 rpm, SAC angle 1°

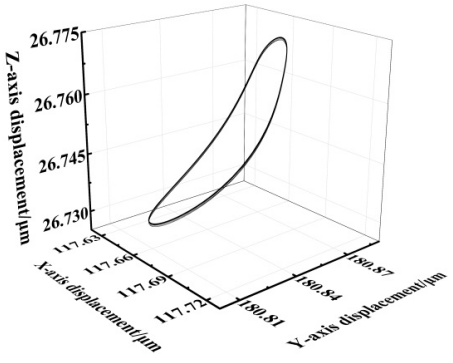

(**e**) Axial load*4, 1600 rpm, SAC angle 1°

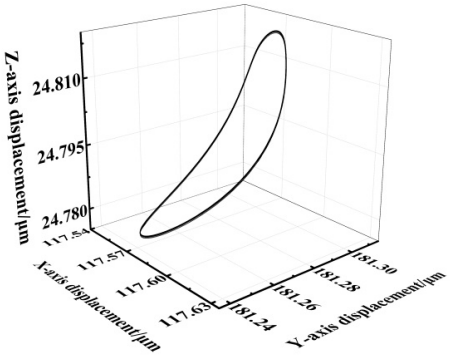

(**f**) Axial*2, 1600 rpm, SAC angle -3°

Figure 20. The motion orbit of the inner ring with different external loads, rotating speeds, and SAC angles.

4.4. Comparisons between the Theoretical and Experimental Results

The experiments were conducted to verify the correctness of the theoretical model as well as the relevant conclusions proposed in this paper. The experimental content includes testing the dynamic performance of 5 kinds of SRBs listed in Figure 9 under the adaptive and limiting operating conditions introduced before in Section 3.3, respectively.

For the adaptive self-aligning operating condition, there are 5 motion orbits of the outer ring relative to 5 different kinds of SRBs in Figure 21a, and the simulating results for ZWZ and SKF bearings are shown in Figure 21b. It can be clearly seen that they have good consistency. Meanwhile, the motion orbits are steady and reliable, namely the SAC angle, which is always located in the allowable range.

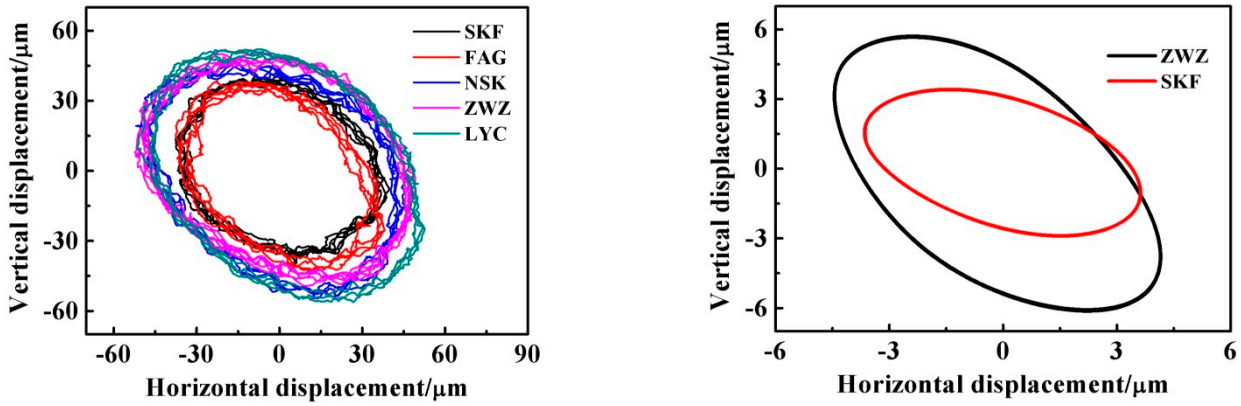

(**a**) Experimental results (**b**) Simulating results for ZWZ and SKF bearings

Figure 21. The motion orbits of SRBs with type 22215 from different manufacturers under adaptive self-aligning operating conditions.

According to the empirical formula given in the bearing manual, the original load is approximately equal to a 22 kN equivalent dynamic load, while 5 times the original load is about 110 kN equivalent dynamic load. In general, the working load should be less than 60% of the equivalent dynamic load in order to withstand random loads and unexpected shocks. So 22 kN represents a light load, and 110 kN represents a heavy load.

Figure 22 shows the displacement vibration spectrum of SRBs. By comparing Figure 22a with Figure 22b as well as Figure 22c with Figure 22d, not only the dominant frequency (namely the times of the roller passing through a certain point of the outer-ring raceway), but also the additional frequencies due to self-aligning function can be coincided both theoretically and experimentally. The values of the dominant and additional frequencies correspond to the description of Equation (51).

Figure 23a reveals the motion orbits of SRBs from different manufacturers under the limiting self-aligning operating condition. Particularly, the SAC angle is limited to 4 degrees. The motion orbits of all the bearings are distorted to different degrees with a larger SAC angle, which is the same as the simulated results shown in the comparison of Figure 23b,c. At this moment, a limitation is regarded as a constraint, so the magnitude of the motion orbit in Figure 23 is obviously smaller than that in Figure 21.

Figure 24 shows the dominant and additional frequencies obtained by the experiment are similar to those computed in the simulation under the SRBs' limiting self-aligning operating condition. Besides, Equation (51) still has the capacity to characterize SRBs with some additional frequency and large amplitude. With the SAC angle under the limiting condition, the additional frequency becomes more obvious, even larger than the dominant frequency revealed in Figure 24a,c. This phenomenon can be used as a characteristic to distinguish SRBs' self-aligning extent.

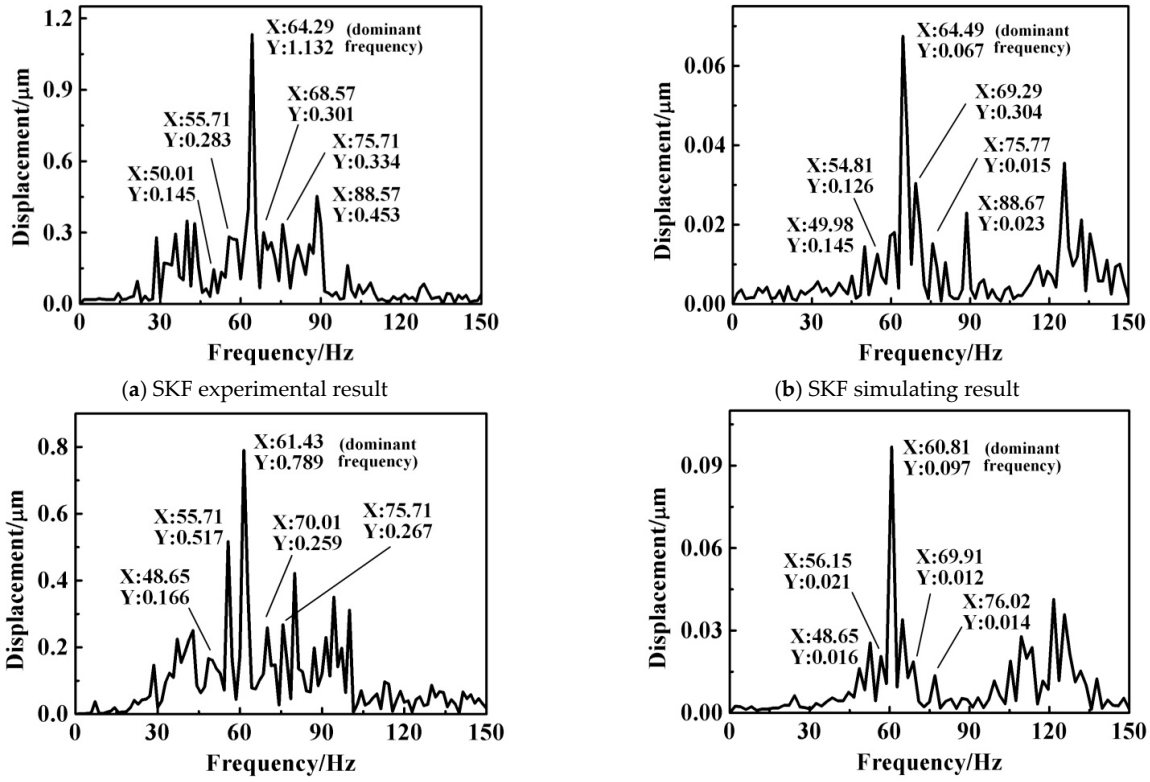

(**a**) SKF experimental result

(**b**) SKF simulating result

(**c**) ZWZ experimental result

(**d**) ZWZ simulating result

Figure 22. The displacement vibration spectrum of SRBs with type 22215 from different manufacturers under adaptive self-aligning operating conditions.

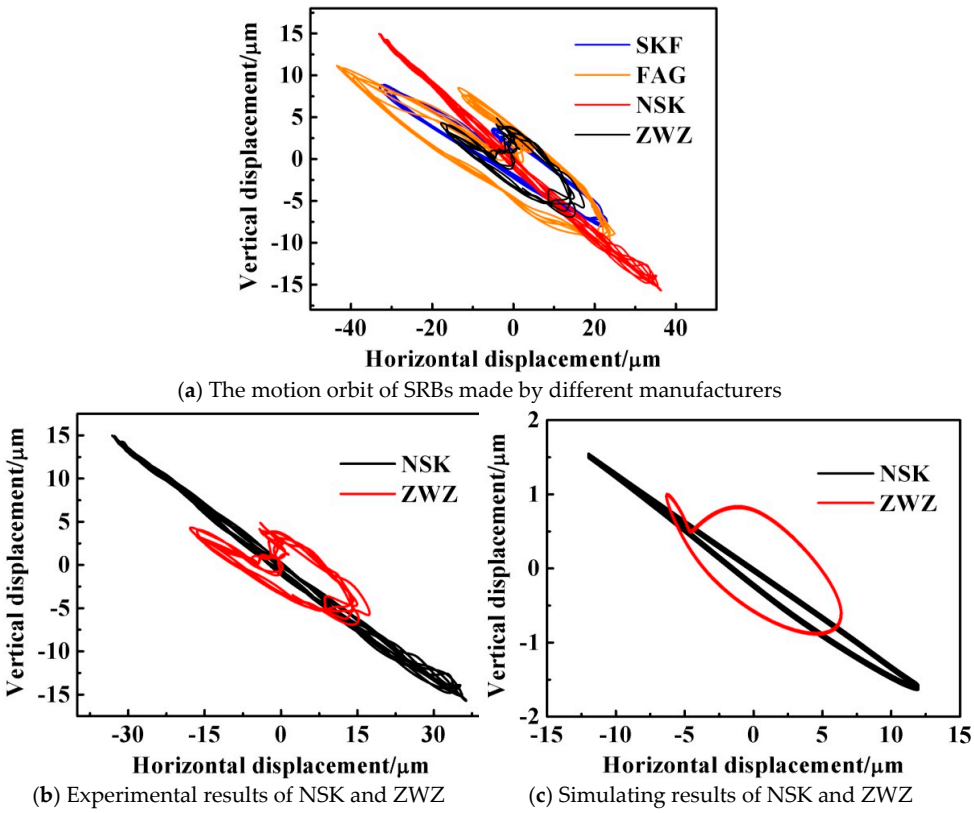

(**a**) The motion orbit of SRBs made by different manufacturers

(**b**) Experimental results of NSK and ZWZ

(**c**) Simulating results of NSK and ZWZ

Figure 23. The motion orbit of SRBs with type 22215 under the limiting self-aligning operating conditions.

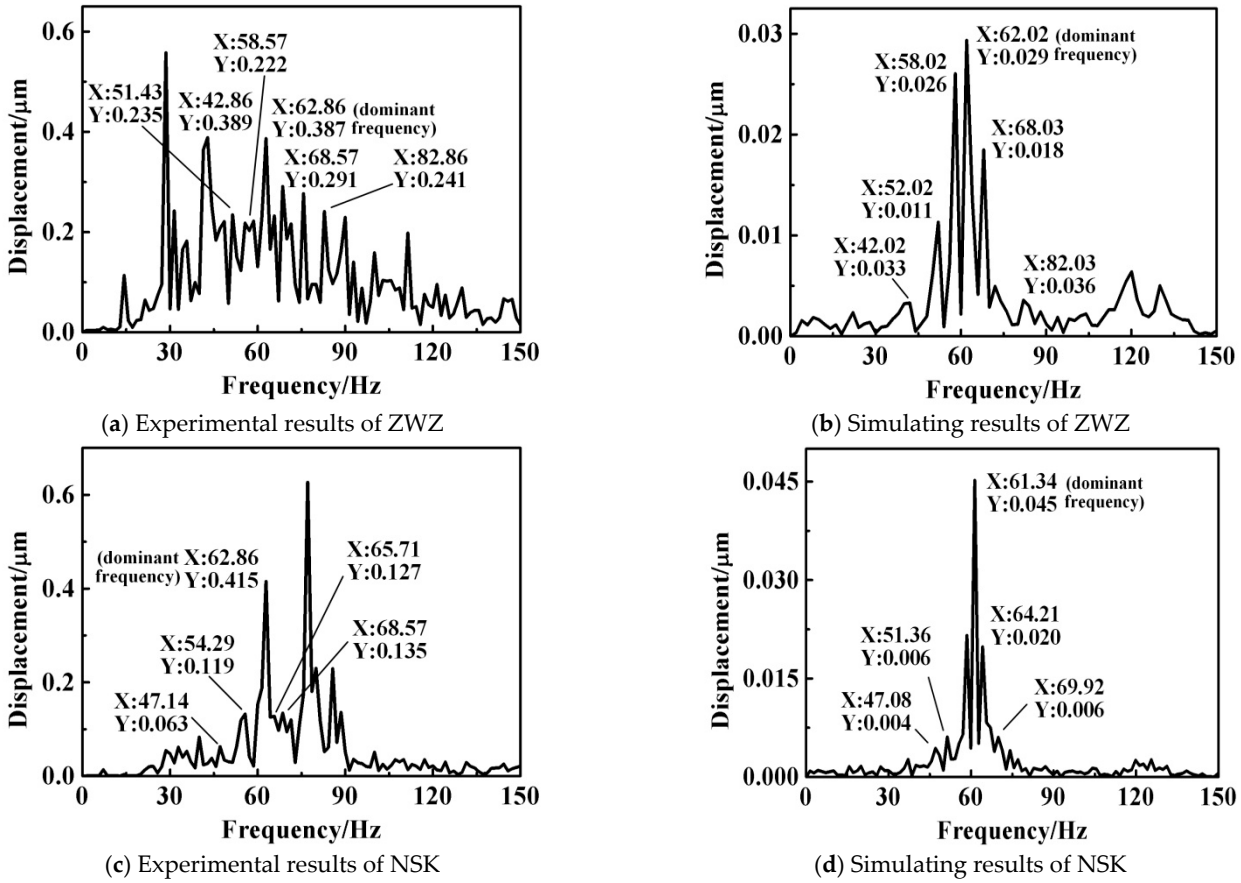

(**a**) Experimental results of ZWZ

(**b**) Simulating results of ZWZ

(**c**) Experimental results of NSK

(**d**) Simulating results of NSK

Figure 24. The displacement vibration spectrum of SRBs from manufacturers ZWZ and FAG under limiting self-aligning operating condition.

5. Conclusions

A theoretical model was proposed based on the Lagrange equation that takes into account the contact status between spheroidal rollers and the raceway, as well as the evaluated method of the SRB's self-aligning contact angle, allowing the dynamic performances of each bearing component to be easily and effectively characterized. A novel pedestal with a self-aligning function was designed to verify the correctness of the theoretical results. And then, in light of the results and discussion, some conclusions are given below.

The amplitude of the inner-ring motion orbit is determined by the external load, but the shape is influenced by the direction and magnitude of the SAC angle. In the example of this paper, the values of the main frequency equal 136.8 Hz. Some additional frequencies are clearly aroused under the self-aligning operating condition, whose value is approximately equal to 8.3 Hz or its integer multiples.

Either the axial load or the self-aligning function will lead to the unbalanced loading of two-row rollers. An oscillation is triggered by a roller entering or leaving the contact region, which is also the reason for the additional frequencies.

The motion orbit of the inner ring will become distorted with a higher rotor speed or improper radial and axial loads. It is not recommended to improve SRBs' dynamic performance purely by increasing the axial load since the unbalanced loading of two-row rollers will emerge. A light axial load plus an anticlockwise self-aligning behavior may achieve a substantial improvement.

The experimental result proves the correctness of the theoretical conclusion. Even if the 5 tested bearings have different geometrical parameters, the characteristics of the main and additional frequencies are the same. In addition, when the SAC angle exceeds the ideal range, the motion orbit is distorted, and the magnitude of the additional frequency is

obviously increasing, even larger than that of the main frequency. This characteristic can be used as an evaluation criterion for the SRB's self-aligning state in condition monitoring.

Author Contributions: Methodology, Y.X. (Yuan Xiao); software, Y.P.; data analysis, Y.Z. (Yin Zhang); investigation, D.Q.; resources, Y.Z. (Yifei Zhang); writing—original draft preparation and review, Y.X. (Yu Xing). All authors have read and agreed to the published version of the manuscript.

Funding: This work was funded by the Key Laboratory of Expressway Construction Machinery of Shaanxi Province (Grant No. 300102251506), the China Postdoctoral Science Foundation (Grant No. 2020M683682XB), the State Key Laboratory of Smart Manufacturing for a special vehicle and transmission system (Grant No. GZ2019KF011) and the Scientific Research Plan Projects of Shaanxi Education Department (Grant No. 22JK0404).

Data Availability Statement: The datasets generated and/or analyzed during the current study are available from the corresponding author upon reasonable request.

Conflicts of Interest: The author declares no conflict of interest in this paper.

References

1. Bercea, I.; Nelias, D.; Cavallaro, G. A unified and simplified treatment of the non-linear equilibrium problem of double-row rolling bearings. Part 1: Rolling bearing model. *Proc. Inst. Mech. Eng. Part J J. Eng. Tribol.* **2003**, *217*, 205–212. [CrossRef]
2. Cao, M.; Xiao, J. A comprehensive dynamic model of double-row spherical roller bearing—Model development and case studies on surface defects, preloads, and radial clearance. *Mech. Syst. Signal Process.* **2008**, *22*, 467–489. [CrossRef]
3. Cao, M. A refined double-row spherical roller bearing model and its application in performance assessment of moving race shaft misalignments. *J. Vib. Control* **2007**, *13*, 1145–1168. [CrossRef]
4. Ghalamchi, B.; Sopanen, J.; Mikkola, A. Simple and versatile dynamic model of spherical roller bearing. *Int. J. Rotating Mach.* **2013**, *2013*, 567542. [CrossRef]
5. Ma, F.; Ji, P.; Li, Z.; Wu, B.; An, Q. Influences of off-sized rollers on mechanical performance of spherical roller bearings. *Proc. Inst. Mech. Eng. Part K J. Multi-Body Dyn.* **2015**, *229*, 344–356. [CrossRef]
6. Yang, J.; Zeng, H.; Zhu, T.; An, Q. Study on the dynamic performance of tilt rotor supported by spherical roller bearings. *Proc. Inst. Mech. Eng. Part K J. Multi-Body Dyn.* **2017**, *231*, 156–166. [CrossRef]
7. Houpert, L. Load-displacement relationships for ball and spherical roller bearings. *J. Tribol.* **2015**, *137*, 021102. [CrossRef]
8. Houpert, L. An engineering approach to Hertzian contact elasticity-part I. *Trans. Am. Soc. Mech. Eng. J. Tribol.* **2001**, *123*, 582–588. [CrossRef]
9. Xing, Y.; Xu, H.; Pei, S.; Chen, X.; Liu, X. A novel non-Hertzian contact model of spherical roller bearings. *Proc. Inst. Mech. Eng. Part J J. Eng. Tribol.* **2016**, *230*, 3–13. [CrossRef]
10. Songyang, J. New Curve Fitting Based Roller Modification Method for Spherical Roller Bearing. In *Journal of Physics: Conference Series, Proceedings of the The 2020 International Conference on Internet of Things, Artificial Intelligence and Mechanical Automation (IoTAIMA) 2020, Hangzhou, China, 10–12 July 2020*; IOP Publishing: Bristol, UK, 2020.
11. Shah, D.B.; Patel, K.M.; Trivedi, R.D. Analyzing Hertzian contact stress developed in a double row spherical roller bearing and its effect on fatigue life. *Ind. Lubr. Tribol.* **2016**, *68*, 361–368. [CrossRef]
12. Fiedler, S.; Kiekbusch, T.; Sauer, B. Investigation of inner contact and friction conditions of a spherical roller bearing using multi-body simulation. *Period. Polytech. Eng. Mech. Eng.* **2011**, *55*, 79. [CrossRef]
13. Ciubotariu, V. Nonconventional Method of Spherical Roller Bearing Design, Using Fea. *Rev. Technol. Neconv.* **2016**, *20*, 30.
14. Steininger, J.; Medvecky, S.; Kohar, R.; Capak, T. Optimization Procedure of Roller Elements Geometry with Regard to Durability of Spherical Roller Bearings. *Commun. Sci. Lett. Univ. Zilina* **2020**, *22*, 68–72. [CrossRef]
15. Li, F.; Qiu, W.B.; Cai, J.B.; Wang, K.; Pan, Z. Analysis of Failure Effect of Cage Thickness on Spherical Roller Bearings. *IOP Conf. Ser. Mater. Sci. Eng.* **2020**, *751*, 012071. [CrossRef]
16. Houpert, L. An enhanced study of the load–displacement relationships for rolling element bearings. *J. Tribol.* **2014**, *136*, 011105. [CrossRef]
17. Houpert, L. An engineering approach to non-hertzian contact elasticity—Part II. *J. Tribol.* **2001**, *123*, 589–594. [CrossRef]
18. Shi, L.; Feng, D.; Xiang, R. Analysis of Maximum Contact Stress of Spherical Roller Bearing in the Case of a Rotating Shaft Deflection. *J. Residuals Sci. Technol.* **2016**, *13*, 263–267.
19. Heikkinen, J.E.; Ghalamchi, B.; Viitala, R.; Sopanen, J.; Juhanko, J.; Mikkola, A.; Kuosmanen, P. Vibration analysis of paper machine's asymmetric tube roll supported by spherical roller bearings. *Mech. Syst. Signal Process.* **2018**, *104*, 688–704. [CrossRef]
20. Kleckner, R.; Pirvics, J. Spherical roller bearing analysis. *J. Lubr. Technol.* **1982**, *104*, 99–108. [CrossRef]
21. Goldstein, H. *Classical Mechanics*; Addison-Wesley: Reading, MA, USA, 1980.
22. Johnson, K.L. *Contact Mechanics*; Cambridge University Press: Cambridge, MA, USA, 1985.
23. Fish, J.; Belytschko, T. *A First Course in Finite Elements*; John Wiley & Sons: Hoboken, NJ, USA, 2007.

24. Huang, P. *Numerical Calculation of Elastohydrodynamic Lubrication: Methods and Programs*; John Wiley & Sons: Hoboken, NJ, USA, 2013.
25. Tandon, N.; Choudhury, A. A theoretical model to predict the vibration response of rolling bearings in a rotor bearing system to distributed defects under radial load. *J. Tribol.* **2000**, *122*, 609–615. [CrossRef]
26. Harris, T.A. *Rolling Bearing Analysis*; John Wiley and sons: Hoboken, NJ, USA, 2001.
27. Harsha, S.; Sandeep, K.; Prakash, R. Non-linear dynamic behaviors of rolling element bearings due to surface waviness. *J. Sound Vib.* **2004**, *272*, 557–580. [CrossRef]
28. Wensing, J.; van Nijen, G. The dynamic behaviour of a system that includes a rolling bearing. *Proc. Inst. Mech. Eng. Part J J. Eng. Tribol.* **2001**, *215*, 509–518. [CrossRef]